

# Development of a photon Monte Carlo radiative heat transfer solver for CFD applications

Georgii Oblapenko<sup>\*†</sup>, Tobias Ecker<sup>\*</sup>, Stefan Fechter<sup>\*</sup>, Tim Horchler<sup>\*</sup>, Sebastian Karl<sup>\*</sup>

<sup>\*</sup>German Aerospace Center (DLR), Bunsenstr a e 10, 37073 G ttingen, Germany  
Address

georgii.oblapenko@dlr.de · tobias.ecker@dlr.de · stefan.fechter@dlr.de · tim.horchler@dlr.de · sebastian.karl@dlr.de

<sup>†</sup>Corresponding author

## Abstract

Radiative heating can play an important role during atmospheric re-entry, combustion processes, and high-enthalpy shock tunnel experiments. The present work details the development of a scalable photon Monte Carlo radiative heat transfer solver based on the open-source SPARTA DSMC code; its verification, coupling with the DLR FlowSimulator framework, and subsequent application.

## 1. Introduction

Accurate simulation of radiative heat transfer is required for multiple aerospace applications: prediction of heat loads on re-entry vehicles,<sup>12,40,41</sup> combustion chambers,<sup>6,9,31,38</sup> and in ablative thermal protection systems,<sup>2</sup> as well as for interpretation of high-enthalpy shock tunnel data.<sup>8,21</sup> Modeling of radiation transport is a computationally expensive task, as radiation emitted in one flow region can have significant impact on faraway flow regions, depending on the optical thickness and local values of the absorption coefficients in the flow. Thus, the non-locality of the problem poses a significant challenge due to the necessity of simulating the mutual interaction between all grid cells in a computation. This is further exacerbated by the need to perform radiation transport computations for all relevant wavelengths at a sufficient spectral resolution, potentially requiring hundreds of thousands of simulations, even when approaches such as opacity binning are used.<sup>22</sup> Finally, coupling between the flow-field and the radiation may need to be accounted for,<sup>5,28,30</sup> which adds yet more computational expense. Therefore, the ability to efficiently conduct accurate simulations of radiative heating is an important prerequisite for high-fidelity simulations of the extreme environments relevant to aerospace research.

Numerous approaches have been developed for simulation of radiative (heat) transfer, such as the tangent slab approximation,<sup>1</sup> the discrete ordinate method,<sup>42</sup> spherical harmonics ( $P_N$ ) method,<sup>17</sup> photon Monte Carlo,<sup>37</sup> as well as hybrid approaches<sup>11</sup> and low-rank methods.<sup>32</sup> Each of them possesses both advantages and disadvantages: inaccuracy of the tangent slab approximation,<sup>28,35</sup> so-called “ray effects” in the discrete ordinate method,<sup>33</sup> lack of fidelity in low-order  $P_N$  methods and high complexity in high-order harmonic-based methods in complicated geometries,<sup>36</sup> and stochastic noise in the photon Monte Carlo approach.

The growing relevance of complex multi-physics simulations in an aerospace context, driven both by engineering challenges and advances in computational power is the motivator for development of a new efficient radiative heat transfer tool intended for use in various aerospace simulations at DLR, with the ultimate goal of it being a radiative heat transfer module for use within the FlowSimulator framework<sup>24</sup> that allows for coupling of various solvers (such as the CFD solvers CODA and HyperCODA,<sup>23</sup> the TRACE turbomachinery flow solver,<sup>14</sup> and other tools, including commercial structural mechanics codes<sup>24</sup>). The photon Monte Carlo method is the simulation approach of choice in the current study, as it is simple both in theory and in implementation, does not exhibit any bias, and whilst subject to stochastic noise, additional simulations can always be performed and the noise levels reduced via ensemble averaging. Moreover, as will be shown below, it allows to leverage existing open-source solutions to an extensive degree. In the present work, an overview of the development, verification and application of the solver is presented, as a first step towards its adoption and use within DLR.

## 2. Photon Monte Carlo

A brief overview of the photon Monte Carlo approach to radiative heat transfer is presented; for more details, the reader is referred to reference literature.<sup>37,45</sup> The whole procedure described below is carried out for each wavelength

## PHOTON MONTE CARLO RADIATIVE HEAT TRANSFER SOLVER FOR CFD APPLICATIONS

(or wavelength bin) of interest (with appropriate emission and absorption coefficients), and as such, within a specific run, the wavelength of the photon bundle does not appear explicitly.

The photon Monte Carlo method models the radiative heat transfer by sampling multiple computational particles (hereafter referred to as “photons”), each of which has a position, velocity, power  $E$ , and transmissivity  $\tau$  associated with it. Assuming no refraction, the magnitude of the velocity is equal to the speed of light in vacuum, and the direction is chosen randomly according to a uniform distribution on a sphere (although approaches utilizing low-discrepancy sequences can also be applied<sup>4</sup>). Similarly, in each grid cell in the calculation, the positions of the photons are assumed to be uniformly distributed. The power emitted in a grid cell (as computed from a spectroscopic code) is distributed equally between all photons in a cell, and at the start of the simulation, each photon has a transmissivity of 1 assigned to it.

The particle tracing code follows each photon as it moves from cell to cell, computing its path length  $ds$  in each cell. As the photon reaches the cell boundary, the length of the photon’s path within that cell is used to update the transmissivity and power:

$$\tau' = \tau \exp(-\kappa ds), \quad (1)$$

$$E' = E \exp(-\kappa ds), \quad (2)$$

where primed variables denote the new values, and  $\kappa$  is the local absorption coefficient in the cell. The power lost by the photon in the cell due to absorption is computed as  $\Delta E = E - E'$  and is added to a tally of power absorbed in each cell. In case  $\alpha'$  becomes lower than some user-defined value threshold value  $\alpha_{\min}$ , the remaining power of the photon is deposited in the cell, and the photon itself is removed from the simulation.

In case of a photon interacting with a surface, it can either be fully absorbed, specularly reflected (potentially losing some fraction of its power to the surface), or diffusely reflected according to Lambert’s cosine law. Similarly, emission of photons from hot surfaces follows Lambert’s cosine law for the photon velocity direction.

Once the photon transport step has been completed, the radiative power emitted in each cell and by each surface element is subtracted from the radiative power deposited in each cell and on each surface element in order to get the local values of the radiative heat source term.

### 3. Implementation

The photon Monte Carlo code was implemented in the open-source SPARTA Direct Simulation Monte Carlo (DSMC) code,<sup>39</sup> developed by Sandia National Laboratories for simulation of rarefied gas flows. The choice of SPARTA as the base code was motivated by two sets of criteria. The first one is related to the **capabilities of the SPARTA code**:

- it is specifically designed for performing particle-based simulations and has all relevant geometric routines implemented (such as particle-surface collisions, axisymmetric remapping, appropriate data structures and algorithms for particle tracking)
- it uses orthogonal (potentially nested) Cartesian grids which allow for efficient particle transport
- it has MPI support and good scaling,<sup>15</sup> as well as support for architecture-agnostic code via the KOKKOS API<sup>10</sup>
- it has an existing Python interface
- it is (relatively) easy to extend SPARTA with new functionality
- it has adaptive grid refinement and dynamic load balancing.

The second set of criteria is related to the **present and planned use of SPARTA within DLR, as well as overall use of SPARTA in academia**:

- SPARTA is already actively used at the Spacecraft Department of DLR for development of a hybrid Fokker-Planck/DSMC approach for plume impingement simulations<sup>3,20,29</sup>
- with the recent additions to the code of force fields and custom per-grid and per-particle data, it is possible to apply SPARTA as a generic particle tracing code by coupling it with flow-field data from other simulation tools
- SPARTA is being actively developed, with bug fixes and new functionality coming not only from the main development team, but also from other research institutions (NASA Jet Propulsion Laboratory, Karlsruhe Institute of Technology, University of Illinois at Urbana-Champaign, DLR, etc.)
- due to its wide use in academia and research, it is possible to get help on its use (via the SPARTA mailing list).

Thus, given the capabilities of the SPARTA code, support for it and continued active development, as well as its history of use within the DLR, it was chosen to be as the most logical starting point of a photon Monte Carlo code. In addition, the existing Python interface simplifies coupling it to other DLR codes (such as the HyperCoda<sup>23</sup> CFD code) within the FlowSimulator<sup>24</sup> framework, which uses Python scripts to perform simulations. It is worth noting that the SPARTA code has already been successfully adapted for radiative heat transfer simulations in porous ablators by the University of Kentucky.<sup>2</sup>

One distinguishing feature of SPARTA is its input script structure: unlike many simulation codes where the input script sets specific code parameters, the SPARTA input commands can be considered a domain-specific programming language (DSL) in itself. The input script is executed sequentially, and the user can re-define commands, change parameters on the fly (for example, one can run a simulation until convergence, perform grid adaptation and subsequent load-balancing, start writing output and then continue the simulation, all fully automated within one input file). As such, extending SPARTA requires writing code that performs these input commands; most of which are belong to the so-called “fix”, “compute”, “collision” or “surface\_collision” categories. Extending these categories is extremely straightforward, however, implementation of the required photon transport functionality is more complicated. Apart from basic implementation of a “Photon” class (with relevant data structures, counters, and photon sampling commands based on grid fields of emission and absorption), several other significant modifications had to be made, due to specifics of both the SPARTA code and the radiative heat transfer problem.

In a parallel SPARTA computation each processor holds information about a subset of grid cells assigned to it (plus a layer of ghost cells, which belong to another a processor but for which the information is known). If during convection a standard DSMC particle reaches the end of a domain block assigned to the processor, it is transferred to another processor (which owns the cell the particle has entered), which then adds it to its list of particles to be convected. As particles do not move much between timesteps (although DSMC is unconditionally stable, basic CFL-like requirements need to be satisfied for convergence<sup>16</sup>), such communication (and the associated overhead) usually occurs for a small fraction of the particles. Photons, however, need to be tracked until they are either fully absorbed or leave the simulation domain. Therefore, unless an optically thick gas is considered, multiple communication steps and ownership handovers might be required for a single photon. For this reason, two significant modifications were made: a photon move routine was written, virtually identical to the standard DSMC particle push routine, except that the photon is tracked throughout the whole domain. This restricts simulations to those where each processor has full knowledge of the whole grid. While storing the full grid information carries additional memory overhead, in radiative heat transfer simulations, relatively coarse grids are normally used (due to the high computational cost and the necessity of performing thousands of line-by-line simulations) and as such, the requirement is not extremely stringent. The second significant change was the introduction of an additional data structure to store the radiative power deposited by the photons in the grid cells. After each convection step, “MPI\_REDUCE“ is called on the global data structure to sum up the radiative source terms computed by the different MPI processes.

Additional changes to the code include new “variable” command options that are used to set grid field data such as black body temperature, absorption coefficients, and emitted power, and to retrieve values of the radiative heat source terms in grid cells and on surface elements. Communication with the FlowSimulator framework is performed using these variables. More details on the implementation of the coupling of SPARTA with the DLR FlowSimulator framework can be found in.<sup>13</sup>

## 4. Numerical results

In this section several radiative heat transfer computations performed with the developed code are presented. These include verification test cases for various aspects of the code (I/O, 2D and axisymmetric simulations, surface emission and absorption, etc.), as well as more complex real-life problems.

### 4.1 Gas inside a channel

The first verification test case assumes a 1-dimensional domain filled with gas; a temperature profile  $T(x)$  of the gas is prescribed and the gas is assumed to emit black-body radiation. The left and right walls also emit black-body radiation with a temperature given by the values of the temperature profile at the left- and right-hand sides of the domain. The problem allows for an analytical solution (the reader is referred to<sup>45</sup> due to the complexity of the equations involved), and is thus a good way to verify multiple aspects of the code’s functionality. For simplicity, a constant absorption coefficient  $\kappa = 1 \text{ m}^{-1}$  was assumed, the domain length was taken to be 1 m, and a parabolic temperature profile was used:  $T(x) = 500 + 2000x - 2000x^2$ . 200 cells were used to discretize the domain.

The left subplot of Fig. 1 shows the computed divergence of the radiative heat flux and the analytical solution with 100 photons emitted per cell and from each wall. A low photon count was used to showcase the noise inherent to

## PHOTON MONTE CARLO RADIATIVE HEAT TRANSFER SOLVER FOR CFD APPLICATIONS

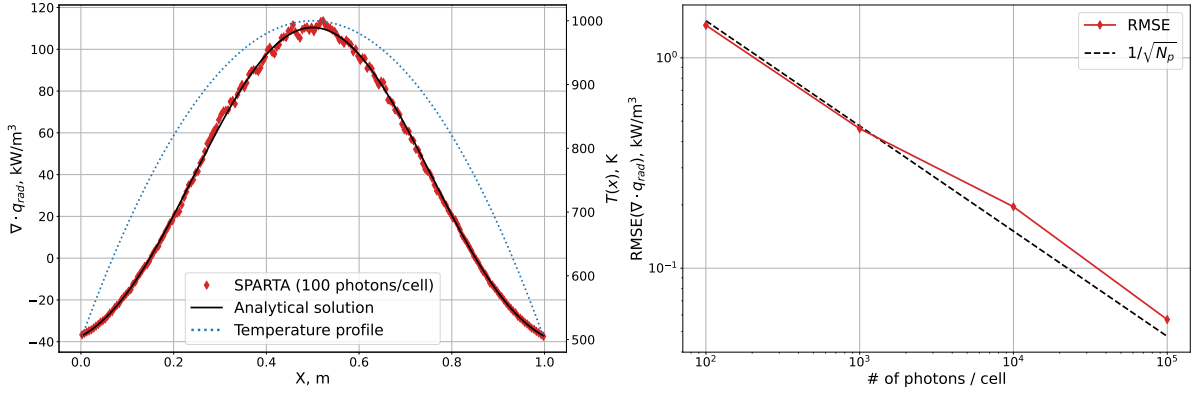


Figure 1: Computed divergence of radiative heat flux and prescribed temperature profile (left) and dependence of simulation error on number of computational photon particles (right).

the Monte Carlo approach; despite the presence of noise, very good agreement with the analytical solution can be seen. Results of a convergence study are shown on the right subplot of Fig. 1. Plotted is the  $L_2$  error between the analytical and computed solution for different numbers of computational photons (per cell) used in the simulation. As expected, the error scales as  $1/\sqrt{N_p}$  (where  $N_p$  is the number of computational photons emitted in each cell).

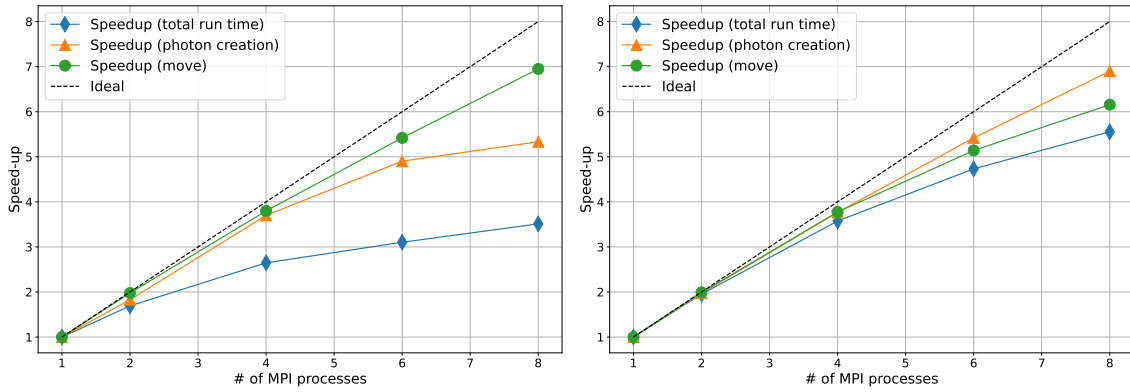


Figure 2: Scaling performance of the code (speed-up compared to serial operation) as a number of MPI processes, 1-D simulation.  $10^4$  photons per cell (left) and  $10^5$  per cell (right).

Figure 2 shows the parallel scaling efficiency of the code for two different numbers of photons emitted per cell. Shown is the speed-up of the whole simulation (“total run time”), the time spent on photon creation (“photon creation”) and the photon convection step (“move”). For  $10^4$  photons emitted per cell (left subplot), the sub-optimal scaling of the total run time is explained by the fact that the code was run for 1 “timestep” (photons were sampled and transported only once), and a non-negligible amount of time (relative to the whole simulation time) is spent on grid construction and MPI communication of grid information (which happen only at the start of the simulation or during grid refinement), and file I/O, which are either serial operations, or operations which require increasing time with increasing process count (grid balancing and communication). If the photon count is increased to  $10^5$  photons per cell, the photon sampling and transport steps become 10 times more computationally expensive, and the role of the code initialization and file I/O operations becomes insignificant. In that case, the total run time scales much better with the number of MPI processes, as can be seen from the right subplot. In a real-life application, the code is expected to be run multiple times on the same grid (for line-by-line simulations or for ensemble averaging), and therefore, the time spent on the set-up operations will be negligible; the FlowSimulator framework also allows for efficient data transfer between computational codes, foregoing the need for the serial text file output used by SPARTA.

#### 4.2 Gas inside an infinite cylinder

The second test-case verifies additional functionality of the code, such as axisymmetric computations and non-uniform grids. A gas emitting blackbody radiation at a constant temperature of 10000 K inside an infinite cylinder of radius 1 m

with fully absorbing (cold) walls is considered.<sup>4,30</sup> The absorption coefficient is taken to be  $\kappa = 1 \text{ m}^{-1}$ .

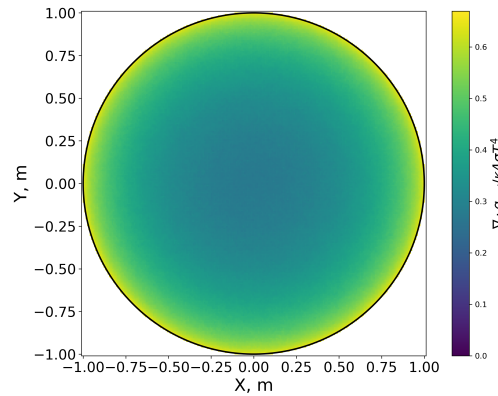


Figure 3: Computed divergence of radiative heat flux inside the cylinder.

An example solution is shown on Fig. 3. The version of the SPARTA code that the radiation transport code is based on does not allow for particle creation in cut cells (grid cells that contain surface elements). Use of a uniform grid would therefore result in a noticeable error in the radiative heat flux near the surface of the cylinder, as no radiation would be emitted from the cells there. To mitigate this issue, the built-in capabilities of SPARTA for grid refinement were used (specifically the option to refine the grid near surface elements) in order to reduce the fraction of the volume inside the cylinder that does not emit radiation. An initial uniform  $50 \times 50$  grid was used, and grid refinement around the cylinder was applied, with the final grid having 4276 cells, out of which 2368 are located fully inside the cylinder.

Due axial symmetry of the problem, it is also possible to avoid using 2D grids and instead simulate a  $1 \times N_y \times 1$  domain (rotated around the  $y = 0$  axis) with periodic boundary conditions in the  $x$  and  $z$  directions. This simulations makes use of the built-in SPARTA capabilities for axisymmetric computations (which require appropriate geometry handling and velocity re-mapping routines). Thus, the simulation cost can be significantly reduced compared to a 2-D simulation. 50 cells were used for the axisymmetric grid. 200 photons per cell were sampled for the 2-D simulation, and 1000 photons per cell were sampled for the axisymmetric computation.

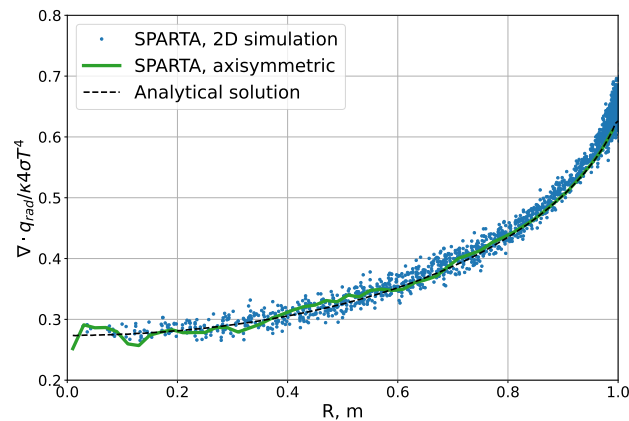


Figure 4: Computed divergence of radiative heat flux inside the cylinder as a function of distance from the center.

Figure 4 shows the computed 2D and 2D axisymmetric solutions along the cylinder radius, along with the analytical solution. Some deviation between the full 2D solution and the analytical solution can be observed near the cylinder wall, due to the aforementioned issue of no photons being emitted in cells with surface elements inside. The axisymmetric solution does not have this problem but does exhibit a higher level of noise near the cylinder center due to the smaller volume of the computational cells.

Figure 5 shows the parallel scaling efficiency of the code for two different numbers of photons emitted per cell. As in the 1-D case, for a lower photon count (left subplot), the total run time scaling is far from ideal. In the 2-D case this is further exacerbated by the grid adaptation routine performed at the start of the simulation. Increasing the photon count per cell to  $10^4$  (right subplot) improves the parallel efficiency of the code, as expected. Of note is the small speed-up observed when increasing the number of MPI processes from 4 to 6. Figure 6 shows the distribution of the

## PHOTON MONTE CARLO RADIATIVE HEAT TRANSFER SOLVER FOR CFD APPLICATIONS

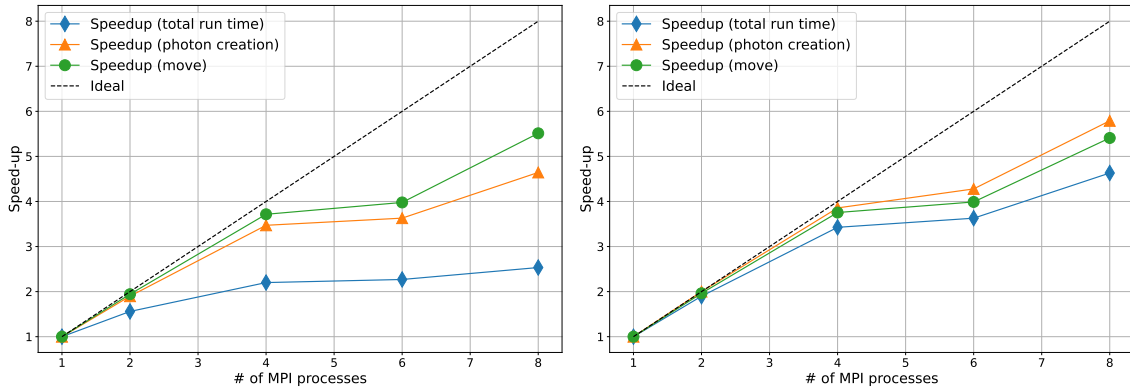


Figure 5: Scaling performance of the code (speed-up compared to serial operation) as a number of MPI processes, 2-D simulation.  $10^3$  photons per cell (left) and  $10^4$  photons per cell (right). RCB load balancing.

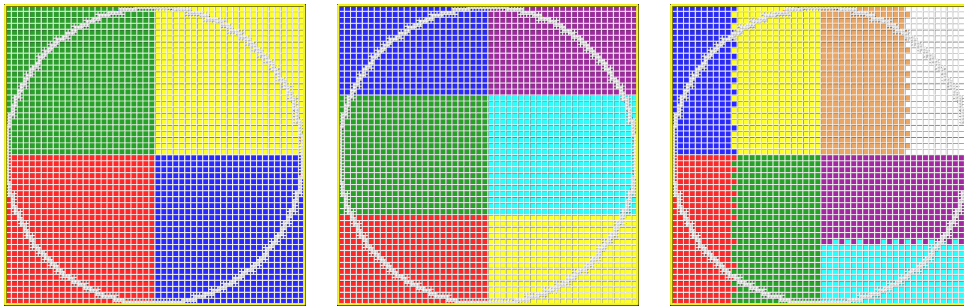


Figure 6: Grid cell distribution amongst MPI processes for 4 (left), 6 (middle), and 8 (right) MPI processes. Different colours of the grid cells correspond to different processes owning the cells.

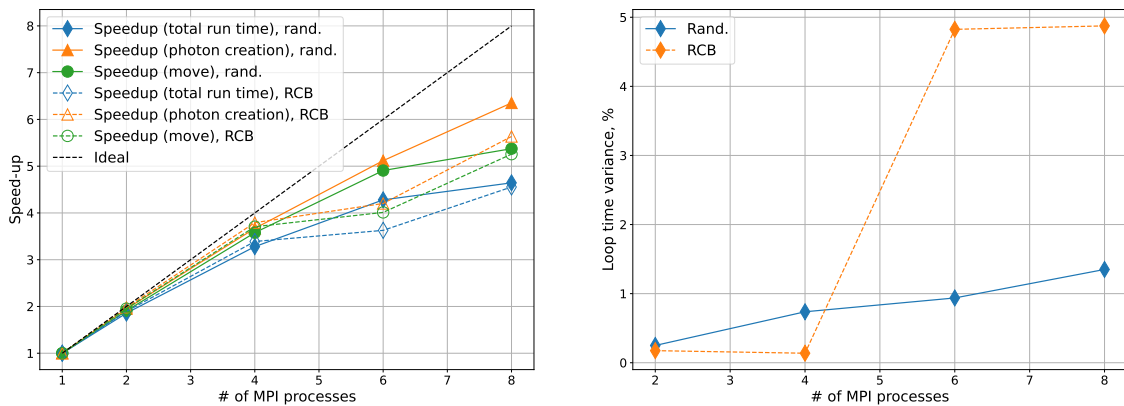


Figure 7: Scaling performance of the code with two different load balancing strategies as a number of MPI processes (left) and variance in convection loop time across processes (right). 2-D simulation,  $10^4$  photons per cell.

grid cells amongst different MPI processes. The recursive coordinate bi-sectioning (RCB) approach is used to assign different cells in the domain to different MPI processes, with the goal of an (approximately) even cell distribution. It can be seen that in the case of 6 MPI processes (middle subplot), the distribution of grid cells inside the cylinder across the processes is quite unequal, with 2 of the processes owning approximately 30% less grid cells inside the cylinder compared to the other 4 processes. Increasing the number of MPI processes to 8 leads to a more even distribution, and better scaling as a consequence. While no new radiation transport-specific load balancing options have been implemented in the code, one other option is to use the random load balancing approach, which assigns cells randomly. Whilst unsuitable for usual DSMC simulations (as particle ownership will change each time a particle exits a cell, leading to very high communication overhead), for the photon Monte Carlo code, where the photons always belong to

the same process, and the grid is not distributed, this might provide improvement over the RCB scheme.

Figure 7 compares the performance of the RCB and random load balancing approaches. It can be seen that the random assignment of cells to MPI processes leads to better performance and less variation in the convection loop execution across processes (as seen on the right subplot). Thus, depending on the specific application, random balancing can be a viable approach for photon Monte Carlo simulations. However, other options may need to be implemented for coupled particle-photon simulations.

### 4.3 Cylinder radiating into vacuum

A third test-case is considered for which an analytical solution is known: an infinite cylinder of radius  $R$  emitting radiation from its surface and a cold (non-emitting and fully absorbing) plate at a distance of  $L$  underneath it; both bodies are assumed to be in vacuum ( $\kappa = 0$ ).

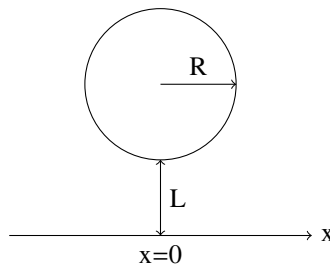


Figure 8: Schematic of problem geometry.

A schematic of the problem geometry is given on Fig. 8. This problem is used to verify the implementation of the surface emission (that uses Lambert's cosine law to sample the directions of the photon velocities). Assuming the center of the cylinder to be located at  $x = 0$ , the heat flux on the plate is given by

$$q(x) = \sigma T^4 \frac{R}{L + R} \frac{1}{1 + \left(\frac{x}{L+R}\right)^2}, \quad (3)$$

where  $T$  is the temperature of the cylinder's surface. In the present work,  $R$  and  $L$  were taken to be equal to 0.5 m, 50 surface elements were used to discretize the cylinder surface, and 120 surface elements were used for the discretization of the top part of the 3 meter long plate. 200000 photons were emitted per surface element.

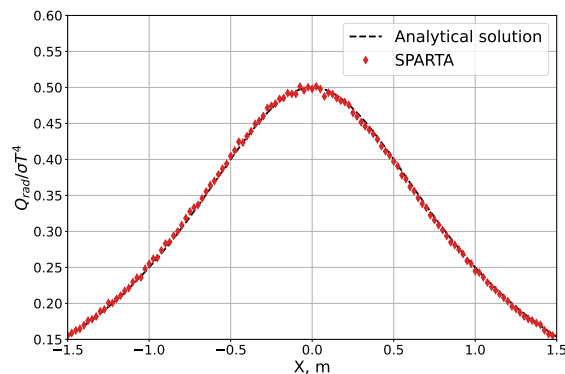


Figure 9: Radiative heat flux distribution on the cold plate underneath the cylinder.

Figure 9 shows the computed radiative heat flux on the surface below the cylinder. Excellent agreement with the analytical solution can be seen, thus verifying the correct implementation of the surface emission procedures.

Figure 10 shows the parallel scaling of the problem in question. Compared to the previous test cases, no volume emission is present, and the only source of photons is the cylinder surface. As can be seen from the left subplot Fig. 10, when the RCB load balancing algorithm is used, the problem does not scale beyond 4 MPI processes (as surface emission is part of the photon transport loop, a separate timer for the photon creation is not available and therefore not plotted). The ownership of the photons does not change throughout a simulation, therefore, only the cores that own

## PHOTON MONTE CARLO RADIATIVE HEAT TRANSFER SOLVER FOR CFD APPLICATIONS

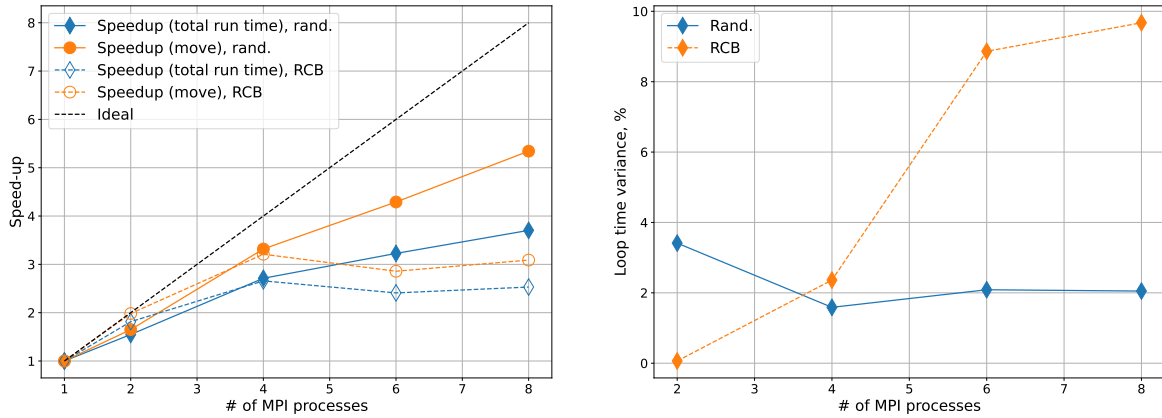


Figure 10: Scaling performance of the code (speed-up compared to serial operation) as a number of MPI processes (left subplot) and and variance in convection loop time across processes (right). 2-D simulation.

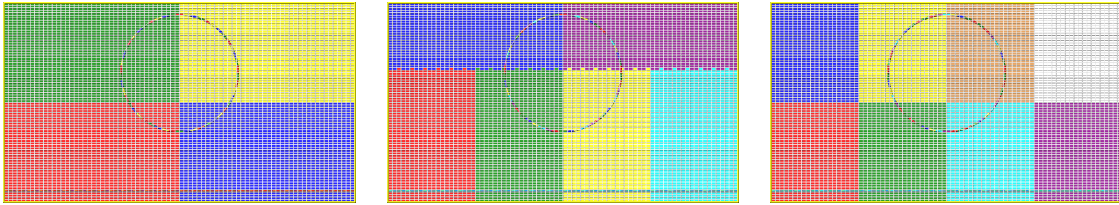


Figure 11: Grid cell distribution amongst MPI processes for 4 (left), 6 (middle), and 8 (right) MPI processes. Different colours of the grid cells correspond to different processes owning the cells.

cells intersecting with the cylinder surface will be performing any actual work (since the cylinder surface is the sole source of photons in the simulation). As such, the load-balancing is far from optimal and the simulation run time does not decrease with an increasing number of cores used. With the random assignment of grid cells to MPI processes, the emitting surface is approximately equally divided among the cores, and the problem scales better. The improvement is also characterized by a significant reduction in variance in the convection loop run-time on each core when using the random grid cell assignment strategy as opposed to the RCB algorithm, as seen on the right subplot of Fig. 10. Figure 11 shows the parts of the domain assigned to different MPI processes (as shown by the different colors) by the RCB algorithm for different total numbers (4, 6, 8) of MPI processes, and it is clearly seen that at most 4 processes will be performing any actual computational work in that case.

Thus, from the last two test cases it is clear that further modifications to the load balancing algorithm are needed to account for the number of photons emitted in each grid block owned by a specific MPI processes and perform grid cell assignment based on this photon count.

#### 4.4 Huygens probe

Although in the limit of an optically thin (Planck average) and optically thick (Rosseland approximation) gas the absorption and emission coefficients can be chosen independently, this is generally not the case for radiating gases occurring in aerospace applications. Thus, it is necessary to compute the spectral emission and absorption independently. A validation test case for the photon Monte Carlo method in the case of independent emission and absorption spectra is the radiative heat flux onto the Huygens satellite<sup>34</sup> during reentry. This test case has already been investigated in detail in previous work<sup>27,30,40</sup> to which we refer for reference. For the comparison of the radiative heat flux we use the spectral binning method<sup>22,44</sup> to simplify the numerical workflow. The underlying idea is to solve the radiation transfer equation for a small number of spectral bins. For these bins specific absorption and emission coefficients were calculated in a pre-processing step and then provided as input to the radiation solver. To simplify the validation, only one single spectral bin is used here that covers the whole frequency range.

To demonstrate and validate our numerical workflow, two computations with the same radiation input data were conducted: one as described in the publications<sup>30,40</sup> using the DLR TAU particle tracer and one using the Photon Monte Carlo method implemented in the SPARTA code. In both approaches the same radiation input in terms of absorption

and emission distributions is used. The approach based on the DLR TAU particle tracer was conducted on the shock-adapted axisymmetric TAU grid while the Photon Sparta approach uses the SPARTA hierarchical grid structure. The variable distribution of the absorption and emission coefficients is done using the general coupling method described in Fechter et al.<sup>13</sup> that allows to couple SPARTA to other field solvers.

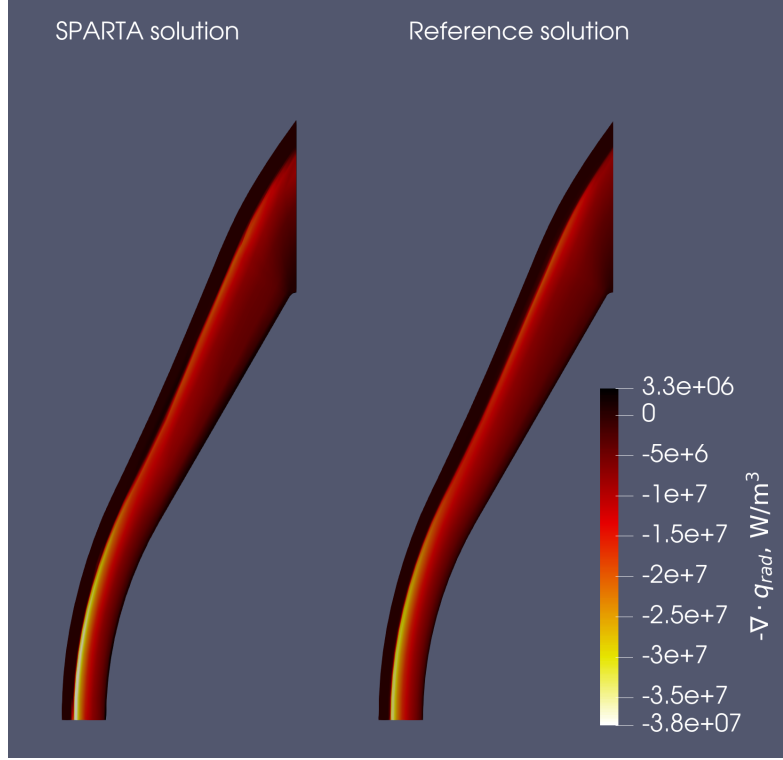


Figure 12: Radiative heat source terms computed by the SPARTA-based code (“SPARTA solution”) and DLR TAU particle tracing code (“Reference solution”).

Figure 12 shows the radiative heat source terms computed by the SPARTA-based photon Monte Carlo code (left) and the DLR TAU particle tracing code (right), using a single spectral bin for simplicity (as the main focus of the work is on verification of the implementation of the coupling, interpolation, and I/O). The SPARTA solution is very close to the one obtained by the DLR TAU radiative transport module, and reproduces all the main aspects of the radiative source term distribution (strong emission immediately after the shock near the stagnation line, weaker emission near the probe’s shoulder, decrease of the magnitude of the radiative source term with decreasing distance to the probe’s surface) very well, both qualitatively and quantitatively.

To better compare the solution obtained with the new code with the reference radiative source term field, we consider the relative difference between the two:

$$\Delta_{rad} = \left| \frac{\nabla \cdot q_{rad,SPARTA} - \nabla \cdot q_{rad,ref}}{\nabla \cdot q_{rad,ref}} \right| \times 100\%. \quad (4)$$

Here  $\nabla \cdot q_{rad,SPARTA}$  is divergence of the radiative heat flux obtained by the SPARTA-based code and  $\nabla \cdot q_{rad,ref}$  is the reference solution produced by the DLR-TAU radiative heat transfer module. Additional processing is performed on  $\Delta_{rad}$ : the difference is set to 0% in areas where absolute value of the radiative source term is less than  $100\text{W/m}^3$ , and differences larger than 100% are clamped down to 100%. This is done to disregard the difference between the solutions in regions with negligible influence of the flow, where the relative difference might be large due to the different grids and interpolation schemes used to carry out the SPARTA-based computation. Figure 13 shows the computed relative difference between the two solutions. Good agreement can be seen in the post-shock region, with the discrepancy being on the order of 2-5%. The largest differences are observed in front of the shock (where the radiative source term is on the order of a few kilowatts per cubic meter, and therefore does not play a significant role) and near the probe’s surface. Differences in front of the shock can be attributed to the non-shock aligned grid used in the SPARTA-based computations, whereas the differences near the surface are also due to the lack of photon emission in cut cells in the SPARTA-based code.

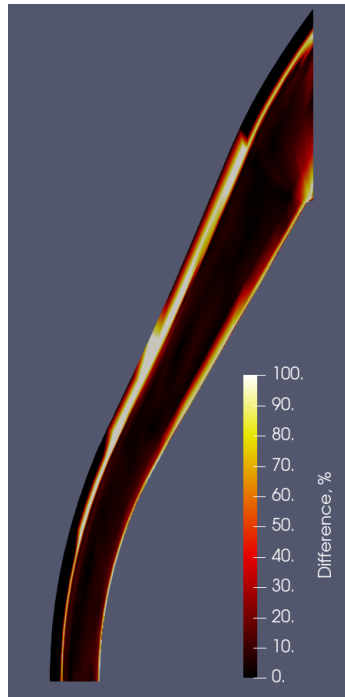


Figure 13: Difference between the radiative heat source terms.

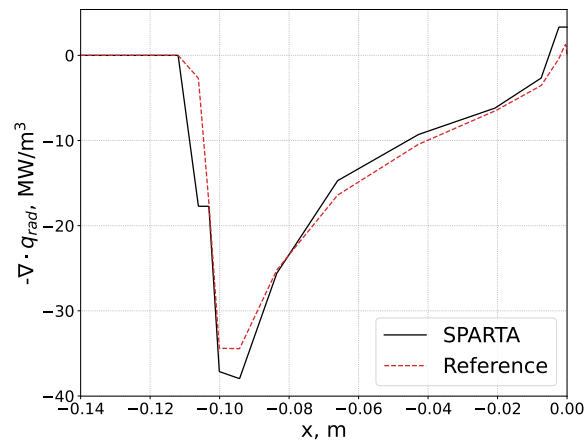


Figure 14: Radiative heat source term along the stagnation line.

Figure 14 shows the radiative heat source term along the stagnation line. As already seen on Fig.13, The SPARTA-based code agrees well with the reference solution, except very close to the body (where emission is underestimated) and in the near-shock region. The planned addition of capabilities to 1) emit photons in grid cells intersected by surfaces and 2) perform adaptive mesh refinement based on the magnitude of the radiative source term is expected to improve the agreement with the reference solution.

#### 4.5 HEG radiative heating anomaly

Finally, the issue of the radiative heating anomaly in the High-Enthalpy Shock Tunnel Göttingen is considered. The radiative heating anomaly is the heat flux augmentation (as compared to expected values) observed in high-enthalpy shock tunnel experiments,<sup>8,25</sup> which can be at least in part explained by radiation emitted by impurities (soot, iron fragments) in the shock layer.<sup>7,25</sup> Additional augmentation might come from the boundary layer in the nozzle or from the reservoir itself, and therefore, the potential role of these sources warrants further investigation. In the present work,

a simplified approach is used to produce an upper bound on the radiative heat flux on a test body due to emission from the reservoir in the High Enthalpy Shock Tunnel Göttingen (HEG)<sup>19</sup> and to study the impact of nozzle surface reflectivity on the thermal load.

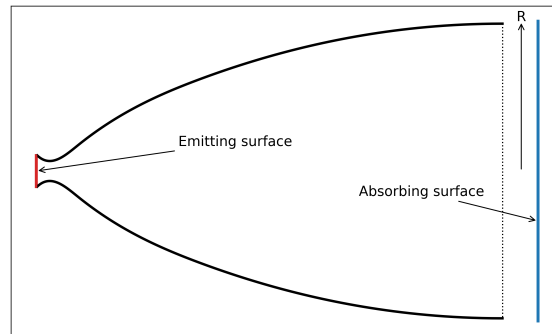


Figure 15: Schematic of the computational setup for analysis of radiation from reservoir.

In the SPARTA-based radiative heat transfer code, an emitting surface is placed at the start of the nozzle. No absorption or additional emission is assumed to happen in the nozzle and the test section (thus, any effects of absorption behind the shock are neglected). A fully absorbing surface is placed in the test section (at a distance of 210 mm from the nozzle exit) that tallies the radiative heat flux. A schematic of the computational setup is shown on Fig. 15 (only the upper half of the domain is actually simulated, as an axisymmetric computation is performed). For further simplification, a black-body emission is assumed from the reservoir with a temperature of 5000 K. The simplifying assumption of no absorption in the flow allows to perform one highly-resolved reference simulation for each surface reflection model using the SPARTA code, and easily recompute the heat flux on the surface in the test chamber for a different value of the emitted radiative heat flux from the reservoir using linear scaling:

$$q_{rad}^*(\mathbf{R}) = q_{rad,ref}(\mathbf{R}) \frac{q_{res}^*}{q_{res,ref}}, \quad (5)$$

where  $q_{rad}^*(\mathbf{R})$  is the new heat flux on the surface,  $q_{res}^*$  is the new heat flux at the end of the reservoir, and  $q_{rad,ref}(\mathbf{R})$  and  $q_{res,ref}$  are the original surface and reservoir end heat fluxes, correspondingly. A more rigorous approach is planned for future work: for a given test condition (reservoir pressure and temperature), the equilibrium chemical composition in the reservoir will be computed (using the Cantera<sup>18</sup> code), along with the effective reservoir length (using the L1D code to estimate the reflected shock speed<sup>26</sup>). These data will then be used to set up a 1-D radiative heat transport problem in the PARADE spectroscopic code<sup>43</sup> and compute the radiative heat flux at the end of the reservoir, which in conjunction with the results obtained for the 5000 K reservoir emission temperature and the scaling relation (5) will allow one to obtain estimates of the impact of radiative heating for different experimental conditions.

Different nozzle surface reflective conditions were tested: 1) a fully absorbing surface 2) surface with specular reflection (with a reflexivity of either 50% or 100%), an 3) surface with diffuse reflection (with a reflexivity of either 50% or 100%).  $10^7$  photons were emitted from the reservoir. For the fully absorbing case, 50000 simulations were carried out — as most photons are absorbed by the nozzle surface and very few of them (approximately 0.05%) reach the nozzle exit plane, a large number of simulations were required to reduce the stochastic noise. For the other cases, 15000 simulations were performed.

Figure 16 shows the radiative heat flux distribution as a function of distance from the nozzle axis. It is evident that the photon-surface interaction model plays a very large role, with the specular reflection leading not only to significant increases in the heat flux (up to more than 20-fold at the centerline and more than 250-fold far away from the axis), but also contributing a strong focusing effect at a distance of approximately 25 cm from the nozzle axis. Thus, direct (non-reflected) radiation from the reservoir leads to moderate heat flux values at the surface (due to the small throat diameter and therefore a very small percentage of the photons being able to pass through without interacting with the nozzle surface), but the contribution of the reflected component is much higher. For the diffuse reflection case, no strong focusing effect is observed, and at most a 4-fold increase in the heat flux is seen for a fully reflecting surface. Therefore, given the strong differences between the results obtained using different reflection models and the high values of the heat flux for some of the cases, further investigation of the problem is warranted, with a more detailed consideration of the nozzle wall reflectivity, incorporation of the radiation from the hot nozzle throat surface, and analysis of the impact of the radiation from the turbulent boundary layer.

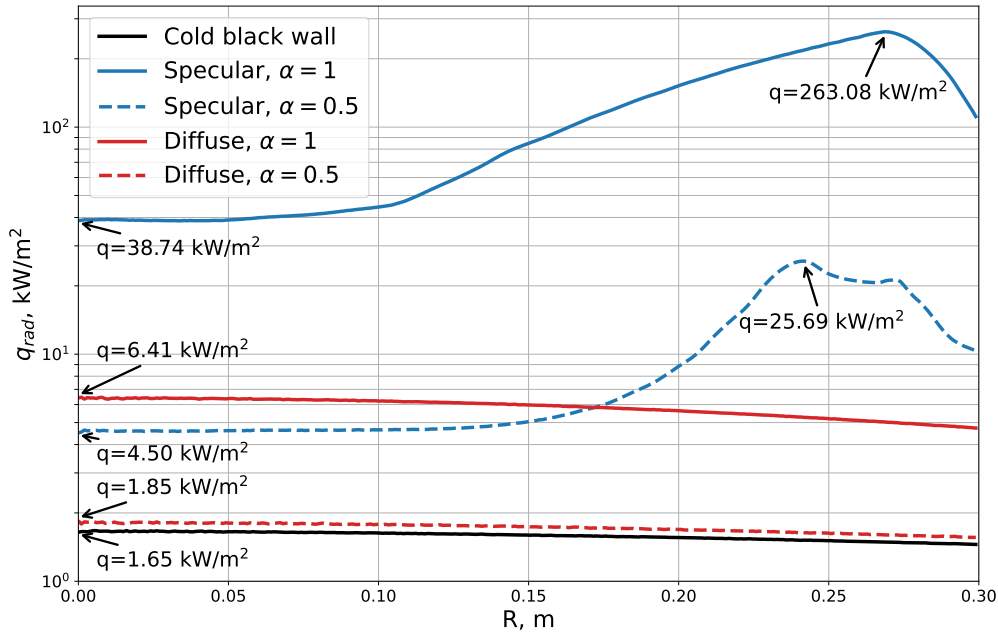


Figure 16: Radiative heat flux distribution on the absorbing surface as a function of the distance from the nozzle axis. Reservoir emission at a black-body temperature of 5000 K.

## 5. Conclusion

An overview of a photon Monte Carlo solver based on the open-source SPARTA DSMC code has been presented, along with several simulations used to verify the implementation of relevant algorithms and test the efficiency of the developed tool. The solver has been successfully coupled to the FlowSimulator framework, and can be used for future simulations.

The solver shows good scaling for small numbers of cores, but additional profiling needs to be performed, along with the implementation of better load balancing options. However, this does not limit its applicability for actual problems of interest. As a large number of radiative transport simulations usually need to be performed (for each spectral wavelength or bin resolved), scaling of the solver to large number of processes may not be required, since the simulations are “embarrassingly parallel” (no communication is required between the computations being carried out for different parts of the spectrum).

Further planned improvements to the photon Monte Carlo solver include: 1) support for adaptive numbers of photons 2) implementation of refraction 3) computation of surface view factors.

## 6. Acknowledgments

Georgii Oblapenko acknowledges the funding provided by the Alexander von Humboldt Foundation for his research stay at the German Aerospace Center (DLR). The authors would like to thank Dr. Divek Surujhlal of the German Aerospace Center (DLR) for helpful discussions on the topic of the radiative heating anomaly.

## References

- [1] John D Anderson Jr. Nongray radiative transfer effects on the radiating stagnation region shock layer and stagnation point heat transfer. Naval Ordnance Lab, White OAK MD, Report 67-104, 1967.
- [2] Ayan Banerjee, Ahmed H Yassin, Raghava SC Davuluri, Alexandre Martin, and Savio J Poovathingal. Radiative coefficients and their influence on in-depth heating of porous ablators. *AIAA Journal*, 60(12):6520–6535, 2022.
- [3] Leo Basov and Martin Grabe. Modeling of polyatomic gases in the kinetic fokker-planck method by extension of the master equation approach (accepted for publication). In *AIP Conference Proceedings*, 2022.

## PHOTON MONTE CARLO RADIATIVE HEAT TRANSFER SOLVER FOR CFD APPLICATIONS

- [4] Julian Beyer, Marcel Pfeiffer, and Stefanos Fasoulas. Non-equilibrium radiation modeling in a gas kinetic simulation code. *Journal of Quantitative Spectroscopy and Radiative Transfer*, 280:108083, 2022.
- [5] Michaela Brchnelová. Radiation modelling in LES for hypersonic flows and combustion systems. MS Thesis, TU Delft, 2020.
- [6] Doyoung Byun and Seung Wook Baek. Numerical investigation of combustion with non-gray thermal radiation and soot formation effect in a liquid rocket engine. *International Journal of Heat and Mass Transfer*, 50(3-4):412–422, 2007.
- [7] Brett A Cruden, Aaron M Brandis, Jay H Grinstead, Joseph Olejniczak, Lindsay Kirk, Randolph P Lillard, Hideyuki Tanno, and Tomoyuki Komuro. Measurement of ultraviolet radiative heating augmentation in Hiest reflected shock tunnel. AIAA Paper 2015-2512, American Institute of Aeronautics and Astronautics, 2015.
- [8] Brett A Cruden, Chun Y Tang, Joseph Olejniczak, Adam J Amar, and Hideyuki Tanno. Characterization of radiative heating anomaly in high enthalpy shock tunnels. *Experiments in Fluids*, 62(7):142, 2021.
- [9] Maria Giuseppina De Flora and Claudio Bruno. Analysis of soot and of its radiative power in supercritical lox/lhc rocket combustion chambers. Number 2005-4439, 2005.
- [10] H Carter Edwards, Christian R Trott, and Daniel Sunderland. Kokkos: Enabling manycore performance portability through polymorphic memory access patterns. *Journal of parallel and distributed computing*, 74(12):3202–3216, 2014.
- [11] K Franklin Evans. The spherical harmonics discrete ordinate method for three-dimensional atmospheric radiative transfer. *Journal of the Atmospheric Sciences*, 55(3):429–446, 1998.
- [12] Elise J Fahy, David R Buttsworth, Rowan J Gollan, Peter A Jacobs, Richard G Morgan, and Christopher M James. Experimental and computational fluid dynamics study of Hayabusa reentry peak heating. *Journal of Spacecraft and Rockets*, 58(6):1833–1846, 2021.
- [13] Stefan Fechter, Immo Huisman, Georgii Oblapenko, Sebastian Karl, Tobias Ecker, and Martin Grabe. Coupling of particle and continuum methods for the simulation of radiative and particle laden flows. Joint 10th EUCASS – 9th CEAS Conference, 2023.
- [14] Martin Franke, Edmund Kügeler, and Dirk Nürnberger. Das DLR-verfahren TRACE: Moderne Simulationstechniken für Turbomaschinenströmungen. *DGLR-Jahrbuch*, 2005.
- [15] Michael A Gallis, John R Torczynski, Steven J Plimpton, Daniel J Rader, and Timothy Koehler. Direct simulation Monte Carlo: The quest for speed. In *AIP Conference Proceedings*, volume 1628, pages 27–36. American Institute of Physics, 2014.
- [16] Michail A Gallis, John Robert Torczynski, Daniel J Rader, and Graeme A Bird. Convergence behavior of a new DSMC algorithm. *Journal of Computational Physics*, 228(12):4532–4548, 2009.
- [17] R DM Garcia, CE Siewert, and JR Thomas Jr. The classical spherical-harmonics method in transport theory. *Transactions of the American Nuclear Society*, 71(CONF-941102-), 1994.
- [18] David G Goodwin, Harry K Moffat, and Raymond L Speth. Cantera: An object-oriented software toolkit for chemical kinetics, thermodynamics, and transport processes, version 2.2. 1. Cantera Developers, Warrenville, IL, 2017.
- [19] Klaus Hannemann, Jan Martinez Schramm, Alexander Wagner, and Giannino Ponchio Camillo. The high enthalpy shock tunnel Göttingen of the german aerospace center (DLR). *Journal of large-scale research facilities JLSRF*, 4(A133):1–14, 2018.
- [20] Christian Hepp, Martin Grabe, and Klaus Hannemann. A kinetic Fokker–Planck approach to model hard-sphere gas mixtures. *Physics of Fluids*, 32(2):027103, 2020.
- [21] Kyle J Higdon, Brett A Cruden, Aaron M Brandis, Derek S Liechty, David B Goldstein, and Philip L Varghese. Direct Simulation Monte Carlo shock simulation of Saturn entry probe conditions. *Journal of Thermophysics and Heat Transfer*, 32(3):680–690, 2018.

## PHOTON MONTE CARLO RADIATIVE HEAT TRANSFER SOLVER FOR CFD APPLICATIONS

- [22] Tim Horchler. Numerical investigation of the shock-generated radiative heat loads on re-entry vehicles. 62nd International Astronautical Congress, 2011.
- [23] Immo Huismann, Stefan Fechter, and Tobias Leicht. HyperCODA—extension of flow solver CODA towards hypersonic flows. In *New Results in Numerical and Experimental Fluid Mechanics XIII: Contributions to the 22nd STAB/DGLR Symposium*, pages 99–109. Springer, 2021.
- [24] Immo Huismann, Lars Reimer, Severin Strobl, Jan Eichstadt, Ronny Tschuter, Arne Rempke, and Gunnar Einarsson. Accelerating the flowsimulator: profiling and scalability analysis of an industrial CFD-CSM toolchain. In *IX International Conference on Computational Methods for Coupled Problems in Science and Engineering*, 2021.
- [25] Tomoaki Ishihara, Yousuke Ogino, Naofumi Ohnishi, and Hideyuki Tanno. Numerical study on abnormal heat flux augmentation in high enthalpy shock tunnel (HIEST). *Transactions of the Japan Society for Aeronautical and Space Sciences*, 58(6):319–326, 2015.
- [26] PA Jacobs. Quasi-one-dimensional modeling of a free-piston shock tunnel. *AIAA journal*, 32(1):137–145, 1994.
- [27] Christopher O Johnston, Brian R Hollis, and Kenneth Sutton. Radiative heating methodology for the Huygens probe. *Journal of Spacecraft and Rockets*, 44(5):993–1002, 2007.
- [28] Christopher O Johnston and Alireza Mazaheri. Impact of non-tangent-slab radiative transport on flowfield–radiation coupling. *Journal of Spacecraft and Rockets*, 55(4):899–913, 2018.
- [29] Eunji Jun, Martin Grabe, and Klaus Hannemann. Cubic Fokker–Planck method for rarefied monatomic gas flow through a slit and an orifice. *Computers & Fluids*, 175:199–213, 2018.
- [30] Sebastian Karl, Daniel Potter, Markus Lambert, and Klaus Hannemann. Computational analysis of radiative heat loading on hypervelocity reentry vehicles. *Journal of Spacecraft and Rockets*, 52(1):63–75, 2015.
- [31] Christoph Kirchberger, Robert Wagner, Hans-Peter Kau, Sebastian Soller, Philip Martin, Marc Bouchez, and Christophe Bonzom. Prediction and analysis of heat transfer in small rocket chambers. AIAA Paper 2008-1260, American Institute of Aeronautics and Astronautics, 2008.
- [32] Jonas Kusch and Pia Stammer. A robust collision source method for rank adaptive dynamical low-rank approximation in radiation therapy. *arXiv preprint arXiv:2111.07160*, 2021.
- [33] Kaye D Lathrop. Ray effects in discrete ordinates equations. *Nuclear Science and Engineering*, 32(3):357–369, 1968.
- [34] J-P Lebreton and DL Matson. The Huygens probe: science, payload and mission overview. *Space Science Reviews*, 104(1-4):59–100, 2002.
- [35] Alireza Mazaheri, Christopher O Johnston, and Siavash Sefidbakht. Three-dimensional radiation ray-tracing for shock-layer radiative heating simulations. *Journal of Spacecraft and Rockets*, 50(3):485–493, 2013.
- [36] Michael F Modest and Shenghui Lei. The simplified spherical harmonics method for radiative heat transfer. In *Journal of Physics: Conference Series*, volume 369, page 012019. IOP Publishing, 2012.
- [37] Michael F Modest and Sandip Mazumder. *Radiative heat transfer*. Academic press, 2021.
- [38] Marco Pizzarelli. Overview and analysis of the experimentally measured throat heat transfer in liquid rocket engine thrust chambers. *Acta Astronautica*, 184:46–58, 2021.
- [39] SJ Plimpton, SG Moore, A Borner, AK Stagg, TP Koehler, JR Torczynski, and MA Gallis. Direct simulation Monte Carlo on petaflop supercomputers and beyond. *Physics of Fluids*, 31(8):086101, 2019.
- [40] Daniel F Potter, Sebastian Karl, Markus Lambert, and Klaus Hannemann. Computation of radiative and convective contributions to Viking afterbody heating. AIAA Paper 2013-2895, American Institute of Aeronautics and Astronautics, 2013.
- [41] I Sohn, Z Li, DA Levin, and MF Modest. Coupled DSMC-PMC radiation simulations of a hypersonic reentry. *Journal of Thermophysics and Heat Transfer*, 26(1):22–35, 2012.
- [42] JS Truelove. Discrete-ordinate solutions of the radiation transport equation. *Journal of Heat Transfer (Transactions of the ASME (American Society of Mechanical Engineers), Series C);(United States)*, 109(4), 1987.

## PHOTON MONTE CARLO RADIATIVE HEAT TRANSFER SOLVER FOR CFD APPLICATIONS

- [43] Michael Winter, Bernd Pfeiffer, Markus Fertig, Monika Auweter-Kurtz, and Arthur Smith. Recent status of the plasma radiation database PARADE. AIAA Paper 2004-2376, American Institute of Aeronautics and Astronautics, 2004.
- [44] AA Wray, JF Ripoll, and D Prabhu. Investigation of the opacity binning approach for solving the shock-generated radiation of the Apollo AS-501 re-entry. In *Proceedings of the Summer Program*, page 187, 2006.
- [45] Yuhui Wu, Michael F Modest, and Daniel C Haworth. A high-order photon Monte Carlo method for radiative transfer in direct numerical simulation. *Journal of Computational Physics*, 223(2):898–922, 2007.